

# Geophysical Research Letters®



## RESEARCH LETTER

10.1029/2024GL113479

## Harnessing Satellite Data Alone for Mapping Global Thermal Anisotropy

Wenfeng Zhan<sup>1,2,3</sup> , Huilin Du<sup>1</sup> , Zihan Liu<sup>1</sup> , Jiufeng Li<sup>1</sup> , T. C. Chakraborty<sup>4</sup>, and Fan Huang<sup>1</sup>

<sup>1</sup>Jiangsu Provincial Key Laboratory of Geographic Information Science and Technology, International Institute for Earth System Science, Nanjing University, Nanjing, China, <sup>2</sup>Jiangsu Center for Collaborative Innovation in Geographical Information Resource Development and Application, Nanjing, China, <sup>3</sup>Frontiers Science Center for Critical Earth Material Cycling, Nanjing University, Nanjing, China, <sup>4</sup>Atmospheric Sciences and Global Change Division, Pacific Northwest National Laboratory, Richland, WA, USA

### Key Points:

- We developed a simple yet effective single-source data-driven approach for global thermal anisotropy mapping
- Surface thermal anisotropy intensity (TAI) holds distinct seasonal and diurnal patterns, with global mean summertime TAI exceeding 2.9°C
- Global mean TAI is closely associated with key surface and atmospheric parameters such as leaf area index and downward shortwave radiation

### Supporting Information:

Supporting Information may be found in the online version of this article.

### Correspondence to:

H. Du,  
[HuilinDu\\_nju@outlook.com](mailto:HuilinDu_nju@outlook.com)

### Citation:

Zhan, W., Du, H., Liu, Z., Li, J., Chakraborty, T. C., & Huang, F. (2025). Harnessing satellite data alone for mapping global thermal anisotropy. *Geophysical Research Letters*, 52, e2024GL113479. <https://doi.org/10.1029/2024GL113479>

Received 9 NOV 2024

Accepted 4 APR 2025

**Abstract** Mapping thermal anisotropy across global lands is critical for advancing a wide range of Earth science studies. However, a comprehensive understanding of global thermal anisotropy intensity (TAI) and its governing factors remains missing. We introduce a novel data-driven methodology to quantify global TAI exclusively using multi-angle MODIS land surface temperature time series observations. Our analysis reveals distinct seasonal and diurnal TAI patterns, with global mean summertime TAI exceeding 2.9°C. Furthermore, we identify strong associations between TAI and key surface and atmospheric parameters, such as leaf area index and downward shortwave radiation. Our findings advocate for a paradigm shift from model-based to data-driven approaches in correcting thermal anisotropy, thereby addressing a critical bottleneck in Earth observation.

**Plain Language Summary** Surface thermal anisotropy refers to the directional dependence of thermal infrared radiation emitted by terrestrial surfaces. Despite decades of scientific inquiry, a comprehensive map of thermal directionality across global lands remains absent. This gap impedes accurate estimation of critical climate variables, and undermines the reliability of a wide range of Earth science studies that are increasingly reliant on satellite-based thermal data. By presenting a novel, statistically robust, data-driven approach that departs from traditional complex model-based methods, we reveal distinct seasonal and diurnal variations in thermal anisotropy intensity (TAI) across global lands, reaching up to 2.9°C during summer days and exceeding 7.0°C in semi-arid regions. We demonstrate evident statistical relationships between TAI and key environmental parameters: leaf area index, terrain elevation variation, air temperature, and incoming solar radiation. Our work addresses a critical gap in our observational capabilities, opening new ways for future investigation of other dynamic and anisotropic terrestrial attributes through satellite remote sensing.

## 1. Introduction

Land surfaces exhibit anisotropic optical properties, reflecting and emitting radiation unevenly in different directions. This phenomenon, well-recognized as non-Lambertian reflectance in the visible spectra (Schaaf et al., 2002), finds its counterpart in the thermal infrared spectra as surface thermal anisotropy (Monteith & Szeicz, 1962; Teng et al., 2023; Wang et al., 2023). Thermal anisotropy substantially hampers the full potential of satellite thermal remote sensing, as current satellite sensors cannot simultaneously capture full hemispherical thermal radiation (Cao et al., 2019). This limitation has been a critical bottleneck for our ability to accurately quantify the Earth's radiation and energy budget (Li et al., 2023). Such a limitation has also adversely affected a wide range of Earth science studies that have been increasingly relying on satellite-derived thermal retrievals (Chakraborty & Qian, 2024; Mildrexler et al., 2011; Schwaab et al., 2021).

Mapping thermal anisotropy across land surfaces globally is crucial to address this limitation. For surface reflectance in the visible spectra, multi-angle satellite observations conducted over short timeframes (e.g., weeks) can help characterize reflectance anisotropy patterns effectively with dedicated satellite orbits (Schaaf et al., 2002). However, multi-angle observations within short timeframes are not applicable for characterizing patterns of thermal radiation anisotropy (Du et al., 2023; Hu et al., 2016; Wang et al., 2022). Surface thermal radiation is influenced not only by the inherent properties of the surface itself, but also by fluctuations in surface temperature that occur within days, hours, or even a few minutes (Cao et al., 2019). These swift temperature

© 2025. The Author(s).

This is an open access article under the terms of the [Creative Commons Attribution-NonCommercial-NoDerivs License](https://creativecommons.org/licenses/by/4.0/), which permits use and distribution in any medium, provided the original work is properly cited, the use is non-commercial and no modifications or adaptations are made.

fluctuations, often orchestrated by changes in atmospheric conditions, complicate efforts to capture a comprehensive view of thermal anisotropy through traditional multi-angle satellite observations.

Physical and semi-physical models have achieved mapping of surface thermal anisotropy regionally and temporally (Bian et al., 2024; Cao et al., 2019, 2021; Jiang et al., 2018; Michel et al., 2023; Qin et al., 2025), but their utility has been constrained by either complex model structure or restrictive assumptions concerning surface temperature dynamics (Text S1 in Supporting Information S1). Recently developed multi-source data-driven approaches offer great mapping potential (Du et al., 2023; Hu et al., 2016; Teng et al., 2023; Wang et al., 2023), yet their reliance on the availability of adjacent water bodies or ground-based observations limits their global implementation (Text S1 in Supporting Information S1). Consequently, our understanding of surface thermal anisotropy remains fragmented across diverse land cover types globally. While associations between thermal anisotropy intensity (TAI, i.e., the maximum thermal radiation difference as quantified by temperature between nadir and off-nadir angles) and environmental factors have been explored regionally (Text S1 in Supporting Information S1), their global consistency remains uncertain. The absence of global-scale statistical associations between TAI and relevant environmental parameters impedes accurate satellite-based thermal retrievals, thereby impacting its applications in various branches of Earth science.

To address the limitations of existing methods, here we developed a simple yet effective single-source data-driven approach for global mapping of thermal anisotropy. Our method harnesses only extensive spatiotemporal averaging of MODIS thermal data, instead of incorporating complex modeling or ground-based data, consequently enabling robust mapping across diverse terrestrial environments, especially for weather conditions that invalidate the restrictive assumption related to surface temperature dynamics and over regions lacking ground-based data. Furthermore, our global mapping provides a basis for investigating the global-scale associations between TAI and key environmental parameters.

## 2. Material and Methods

### 2.1. Data Sets

*Data sets for thermal anisotropy mapping across global lands.* Multi-angle land surface temperature (LST) observations derived from Aqua and Terra MODIS products spanning from 2003 to 2022 were employed for mapping global land surface thermal anisotropy (Text S2 in Supporting Information S1). The influence of land cover change during the study period has been demonstrated to be minimal (Text S3 in Supporting Information S1). The chosen MODIS LST data sets possess several benefits, including relatively high temporal resolution (daily) and spatial resolution (1 km at nadir), an extensive temporal archive covering over two decades, and established high accuracy. The MODIS sensors capture a wide range of viewing zenith angles (VZA) from  $-65^\circ$  to  $65^\circ$ , with a 16-day revisit period for each surface location. These attributes make the MODIS data sets particularly well-suited for studies on thermal anisotropy (Du et al., 2023; Hu et al., 2016; Teng et al., 2023; Wang et al., 2023). LST observations from the MOD11A1 product were acquired at approximately 10:30 a.m. and 22:30 p.m., while those from the MYD11A1 product were obtained at approximately 13:30 p.m. and 01:30 a.m.

*Data sets for examining relationships between thermal anisotropy intensity (TAI) and several surface and atmospheric parameters.* We selected four surface and two atmospheric parameters to examine their relationships with TAI globally. Surface parameters include leaf area index (LAI) from the MCD15A3H product (4-day; 500 m), enhanced vegetation index (EVI) from the MOD13A2 product (16-day; 1 km), tree cover percentage (TCP) from the MOD44B product (yearly; 250 m), and standard deviation of elevation ( $\sigma_{\text{ele}}$ ) from the SRTMGL1\_003 product (30 m). Sensitivity analyses indicate that the potential impacts from retrieval errors in MODIS products should be relatively minimal (Text S4 in Supporting Information S1). Atmospheric parameters include hourly downward shortwave radiation (RAD) and surface air temperature (SAT) provided by the reanalysis ERA5-land product ( $\sim 9$  km). We further converted the Coordinated Universal Time (UTC) of RAD and SAT data to local solar time. To ensure data consistency, all data sets were retrieved during a common temporal period (2003–2022) and resampled to a spatial resolution of 1 km to match the MODIS LST product.

### 2.2. Mapping Thermal Anisotropy Across Global Lands

Through dedicated satellite orbits, multi-angle satellite observations acquired over short time periods (e.g., days or weeks) can be effectively used to characterize anisotropy in surface reflectance (Schaaf et al., 2002). Unlike

characterization of reflectance anisotropy, thermal radiation is jointly controlled by VZA and rapid LST variations resulting from fluctuating atmospheric conditions (Cao et al., 2019). This joint control poses a significant challenge for mapping of thermal anisotropy using multi-angle LST observations from polar-orbiting sensors, mostly because such multi-angle observations are usually collected at different times and dates.

The cornerstone of mapping thermal anisotropy is to maximize the LST variations in accordance with VZA variations (typically 3.0–5.0°C during the day), while minimizing the influence of LST changes due to fluctuating atmospheric conditions (often exceeding 10.0°C within a single day or a single season). Previous studies have addressed this challenge by incorporating diurnal LST cycle models (i.e., semi-physical models or dynamic kernel-driven models) or by using auxiliary ground-based observations (i.e., multi-source data-driven models; Text S1 in Supporting Information S1). However, the restrictive assumptions related to modeling LST dynamics or additional ground-based observations in these studies significantly limits their applicability over various weather conditions that could invalidate the assumptions related to diurnal temperature dynamics as well as across diverse global landscapes where such data are scarce or even entirely absent.

In fact, direct averaging of LST observations acquired at various VZAs is also a simple yet effective solution to minimize LST variations induced by fluctuating atmospheric conditions. For example, by averaging approximately 50 valid observations within each specific VZA bin, the disturbance from atmospheric fluctuations (typically 10.0°C) can be rapidly reduced to less than 1.5°C, according to the Bessel formula in error theory (Pugachev, 2014). This reduced disturbance by simple averaging (i.e., 1.5°C) is substantially smaller than the TAI of most surfaces, therefore allowing for direct mapping of thermal anisotropy without any complex modeling or auxiliary data. Nevertheless, the TAI derived from this approach represents an average across various atmospheric conditions and, as such, may be lower than the TAI at a specific instantaneous moment.

We need to underscore that data preprocessing procedures are required before the direct averaging of satellite thermal observations, because LST data are often subjected to uncertainties arising from LST retrieval and additional anomalies. Therefore, we proposed a simple yet effective single-source data-driven methodology for mapping thermal anisotropy across global lands. This comprises a rigorous four-step process: (a) removal of outliers in LST observations and binning of VZAs; (b) further exclusion of LST anomalies and careful selection of valid VZA bins; (c) calculation of TAI; and (d) uncertainty analysis related to the potential impacts from retrieval errors in LSTs, land cover changes during the study period, and directionalities of both atmospheric attenuation and emissivity. More details are provided in Texts S2–S5 in Supporting Information S1. Using this methodology, we mapped thermal anisotropy across global lands for both summer and winter. Summer (winter) was defined as June to August (December to February) in the Northern Hemisphere while December to February (June to August) in the Southern Hemisphere.

### 2.3. Examination of Relationships Between TAI and Surface and Atmospheric Parameters

To enable practical angular normalization of thermal anisotropy across global lands, we examined the associations between TAI and key surface and atmospheric parameters (Figure S1 in Supporting Information S1). This included quantifying TAI variations for each selected parameter, as well as analyzing TAI variations for several parameters. With such quantified associations, angular normalization can directly be performed for each pixel once surface and atmospheric parameters are known.

*Selection of key surface and atmospheric parameters.* Previous studies have shown that TAI is closely related to surface properties (e.g., vegetation and topography) and atmospheric conditions (e.g., solar radiation and air temperature) (Duffour, Lagouarde, & Roujean, 2016; Ermida et al., 2017, 2018; Jiao et al., 2019; Rasmussen et al., 2010; Trigo et al., 2008; Wang et al., 2023; Yan et al., 2016). Considering the global availability of relevant data sets and the extensive terrestrial coverage of vegetation and mountainous terrain (Teng et al., 2023), we selected LAI, EVI, and TCP as surface parameters for representing vegetation status, while chose  $\sigma_{\text{e}}$  to represent topography. Furthermore, we incorporated RAD and SAT within a 2-hr window preceding the satellite overpass as atmospheric variables (Du et al., 2023).

*Examination of TAI variations with surface parameters.* The core of analyzing TAI variations with surface parameters lies in incorporating the spatial information from multiple pixels. We conducted a two-step analysis to assess the relationship between TAI and surface parameters. First, LST pixels were categorized into groups based on ascending parameter values, with each group representing a distinct surface property. For instance, LAI values

were divided into nine intervals ranging from 0 to 4.5 in 0.5 increments. Second, mean TAI was calculated for each group, and TAI variations depending on each surface parameter were then examined across each climate zone. Our sensitivity analyses indicated that the main findings are relatively insensitive to the choice of interval number (Text S6 in Supporting Information S1).

*Examination of TAI variations with atmospheric parameters.* In contrast to the relationship between TAI and surface parameters, the core of examining TAI variations with atmospheric parameters involves utilizing the temporal information from individual pixels. To assess the relationship between TAI and atmospheric parameters, we conducted a three-step analysis. (a) Categorization of atmospheric conditions: Given the relatively close atmospheric status at neighboring pixels, atmospheric conditions were categorized using a  $2^\circ \times 2^\circ$  grid to enhance computational efficiency. Within each grid, daily SAT and RAD values from within 2 hours prior to satellite overpasses were extracted from reanalysis data and subsequently masked using MODIS LST observations to obtain their clear-sky values. We then categorized all daily SAT or RAD values into eight classes based on their ascending values for each season (Text S6 in Supporting Information S1), with each class representing a specific type of atmospheric condition. (b) Quantification of TAI under each atmospheric condition: TAI was averaged for each atmospheric condition category by matching corresponding dates with MODIS LST data. (c) Analysis of TAI variations with SAT or RAD for each climate zone: SAT and RAD exhibit spatial variability both among different dates and across grid locations due to underlying climatic conditions (Figure S2 in Supporting Information S1). Therefore, it is essential to account for regional climatic differences to accurately examine TAI variations depending on SAT and RAD values induced by variations in weather conditions. This implies that the grids used for quantifying TAI under each category of atmospheric condition must be identical. Therefore, we further selected the grids with common temporal RAD or SAT intervals within each climate zone and investigated TAI variations using these meticulously chosen grids (Figure S3 in Supporting Information S1). This approach did minimize the impact of regional climatic differences, yet it led to narrower ranges of RAD and SAT values for analysis (e.g., 400 to 900 W/m<sup>2</sup> for equatorial RAD in Figure 3d).

*Examination of TAI variations with the interplay of one surface parameter and one atmospheric parameter.* To investigate TAI variations with the interplay of surface and atmospheric parameters, we integrated spatial and temporal information across multiple pixels. For a given region, LST data from multiple pixels were first categorized temporally based on daily atmospheric information, generating distinct LST categories representing specific atmospheric conditions. These LST categories were then further subdivided spatially according to surface parameter values. This method allows for a comprehensive examination of TAI variations with the interplay of surface and atmospheric parameters. Our analysis based on carefully selected grids indicated that TAI is more strongly related to SAT than RAD (Figures 3c and 3d; the underlying explanations for this phenomenon are provided in Text S7 in Supporting Information S1). We therefore chose SAT as the atmospheric parameter with either LAI or  $\sigma_{\text{ele}}$  as the surface parameter to explore the interactive effects. As an example, we analyzed the associations between TAI and the interplay of SAT-LAI in the equatorial region, as well as between TAI and the interplay of SAT- $\sigma_{\text{ele}}$  over the Tibetan Plateau. For the case in the equatorial region, LST observations within a season were categorized into eight groups based on SAT values, and each SAT group was further subdivided into nine LAI-based groups, resulting in 72 LST subsets (i.e.,  $8 \times 9 = 72$ ) representing unique combinations of surface and atmospheric conditions. TAI was then calculated for each subset to assess its variation with both SAT and LAI. Analysis of the associations between TAI and SAT- $\sigma_{\text{ele}}$  in the Tibetan Plateau followed a similar procedure.

### 3. Results

#### 3.1. Thermal Anisotropy Intensity Maps Across Global Lands

Our analysis reveals distinct seasonal and diurnal patterns in TAI across global lands (Figure 1; Figure S4 in Supporting Information S1). Summer displays a stronger TAI than winter (Figures 1c and 1d). Diurnally, TAI demonstrates a pronounced peak at approximately 13:30 (Aqua daytime transit), followed by that around 10:30 (Terra daytime transit) (Figures 1c and 1d). In contrast, substantially lower TAI values are observed during the nighttime transits at around 22:30 (Terra) and 01:30 (Aqua) (Figures 1c and 1d). During summer days, the global mean TAI reaches 2.7°C in the morning and 2.9°C in the afternoon (Figures 1a and 1d). These values represent approximately half of those observed over global cities (Du et al., 2023), likely due to the higher heterogeneity and more pronounced three-dimensional urban geometries compared to natural landscapes (Stewart & Oke, 2012). The hotspots (i.e., the observation angle where the strongest thermal radiation occurs) in thermal

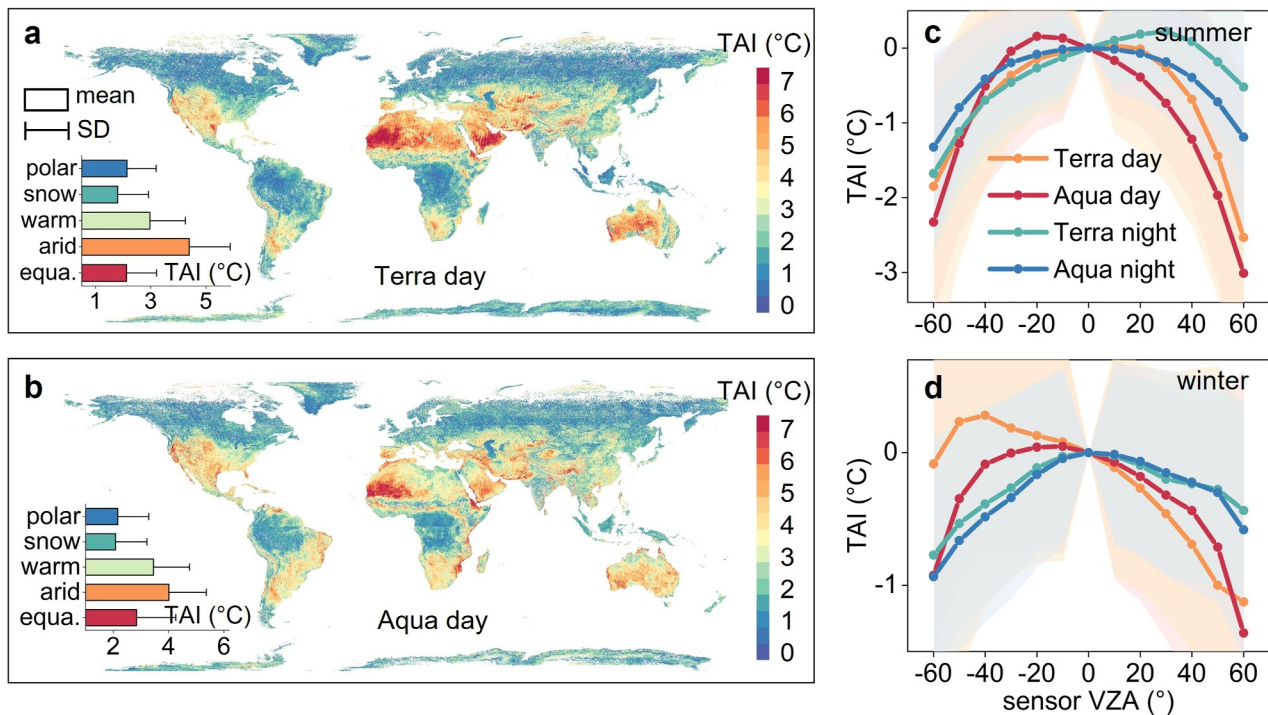


**Figure 1.** Global spatial patterns on thermal anisotropy intensity (TAI) during summertime from 2003 to 2022. Spatial distribution of TAI during summer daytime, differentiated by morning (Terra day; a) and afternoon (Aqua day; b); TAI curves for different sensor viewing zenith angles (VZAs) at four diurnal times during summer (c) and winter (d).

anisotropy curves during summer days coincide well with the theoretical average sun positions—the hotspots exhibit zenith angles ranging from  $+15^\circ$  to  $+25^\circ$  (i.e., eastern direction) for morning and from  $-25^\circ$  to  $-15^\circ$  (i.e., western direction) for afternoon (Figure 1c).

Spatially, arid regions exhibit the highest mean TAI ( $4.2^\circ\text{C}$ , averaged across summer mornings and afternoons, and similarly below), followed by warm regions ( $3.3^\circ\text{C}$ ). In contrast, equatorial ( $2.5^\circ\text{C}$ ), polar ( $2.2^\circ\text{C}$ ), and snow regions ( $2.0^\circ\text{C}$ ) demonstrate notably lower mean TAI values (Figures 1a and 1b; Figure S5 in Supporting Information S1). The enhanced TAI in arid regions is likely attributable to higher solar shortwave radiation received by their land surfaces (Figure S2 in Supporting Information S1), which amplifies temperature disparities among various surface components, leading to stronger thermal anisotropy observed in these regions. Within arid regions, TAI displays further spatial variability (Figure 2). Sandy surfaces show a stronger TAI ( $7.1^\circ\text{C}$ ) compared to mountainous ( $2.6^\circ\text{C}$ ) or plateau ( $4.7^\circ\text{C}$ ) surfaces (Figure 2; Figure S6 in Supporting Information S1), which are often characterized by stony or rocky landscapes. This observation aligns with recent reports for the Sahara Desert concluded from Sentinel-3 LST observations (Ermida et al., 2024). Our analysis of potential drivers of TAI patterns over this region (Figures S7 and S8 in Supporting Information S1) suggests that the enhanced TAI over sandy surfaces is likely due to the presence of undulating sand dunes (Figure S9 in Supporting Information S1) and the lower specific heat capacity of sand. This combination of factors in deserts, together with the pronounced solar radiation over arid regions, leads to greater temperature differences between sunlit and shaded components compared to mountainous and plateau terrains. Despite potential uncertainties in LST retrievals over hot and dry surfaces, the reliability of these findings has been validated through additional sensitivity analyses (Text S8 in Supporting Information S1).

Furthermore, we observe a notable west-to-east horizontal line of relatively low, then high, and then low TAI patterns from north to south at approximately  $10^\circ\text{N}$  near the Sahara Desert, which may be related to the land cover transition from grasslands to savannas (Rasmussen et al., 2010; Figures S10–S12 in Supporting Information S1). In northern regions dominated by grasslands, the terrain is relatively uniform with minimal elevation variation, resulting in lower TAI. In the central region where grasslands gradually transit to savannas, the inclusion of both grasslands and trees increases elevation variation, enhancing the temperature contrast between sunlit and shaded

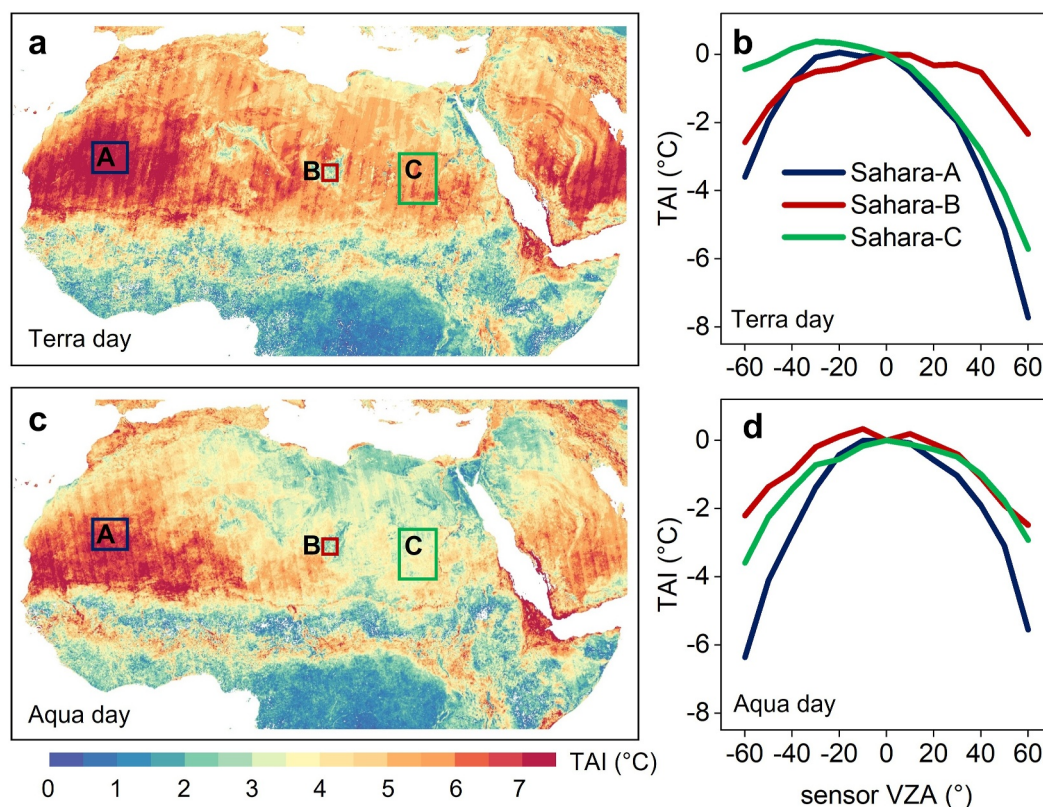


**Figure 2.** Spatial distribution of TAI during summer daytime across the Sahara Desert. Spatial distribution of TAI during summer morning (a) and afternoon (c); TAI curves for different sensor VZAs (b and d) over three typical surface types within the Sahara Desert, including surfaces covered mainly by pure deserts (termed Sahara-A), mountains (Sahara-B), and plateaus (termed Sahara-C).

areas and raising TAI. By contrast, in the southern areas dominated by tropical savannas, the higher proportion of trees reduces elevation variation, leading to lower TAI.

### 3.2. Relationships Between TAI and Key Surface and Atmospheric Parameters

Our analysis of surface and topographic variables reveals a consistent negative correlation between TAI and LAI across various climatic zones (Figure 3a; Figures S13a and S13d in Supporting Information S1). This inverse relationship also extends to TCP (Figures S13b and S13e in Supporting Information S1). Nevertheless, the association between TAI and EVI is more complex, exhibiting an initial increase followed by a decrease, with a turning point around 0.1 (Figures S13c and S13f in Supporting Information S1). This divergence may be attributed to EVI's reliance on spectral reflectance, allowing it to be measured even in non-vegetated regions. Notably, EVI values below 0.1 typically correspond to bare soil or rocky surfaces (Alexandridis et al., 2020), which often exhibit lower TAI values (Cao et al., 2019). Across climatic zones in mountainous regions worldwide, TAI generally increases with increasing  $\sigma_{ele}$  across climatic zones (Figure 3b; Figures S14 and S15 in Supporting Information S1). However, a slight decrease may be observed at low  $\sigma_{ele}$  values, likely resulting from the complex interplay of topography and solar radiation. In mountainous regions with relatively gentle topography (typically at lower elevations), surfaces tend to receive greater solar radiation (Figure S16 in Supporting Information S1), potentially making its influence on TAI more pronounced than that of topography. Consequently, as  $\sigma_{ele}$  increases, the reduction in solar radiation may lead to a slight decline in TAI.

Examining atmospheric variables, our analysis demonstrates that larger TAI values are consistently associated with higher SAT and stronger RAD across various climatic zones, yet with the correlation between TAI and SAT being more pronounced within the selected grids (Figures 3c and 3d; Figure S17 in Supporting Information S1). We further explored the interactive effects of SAT with LAI and SAT with  $\sigma_{ele}$  on TAI in specific regions. For

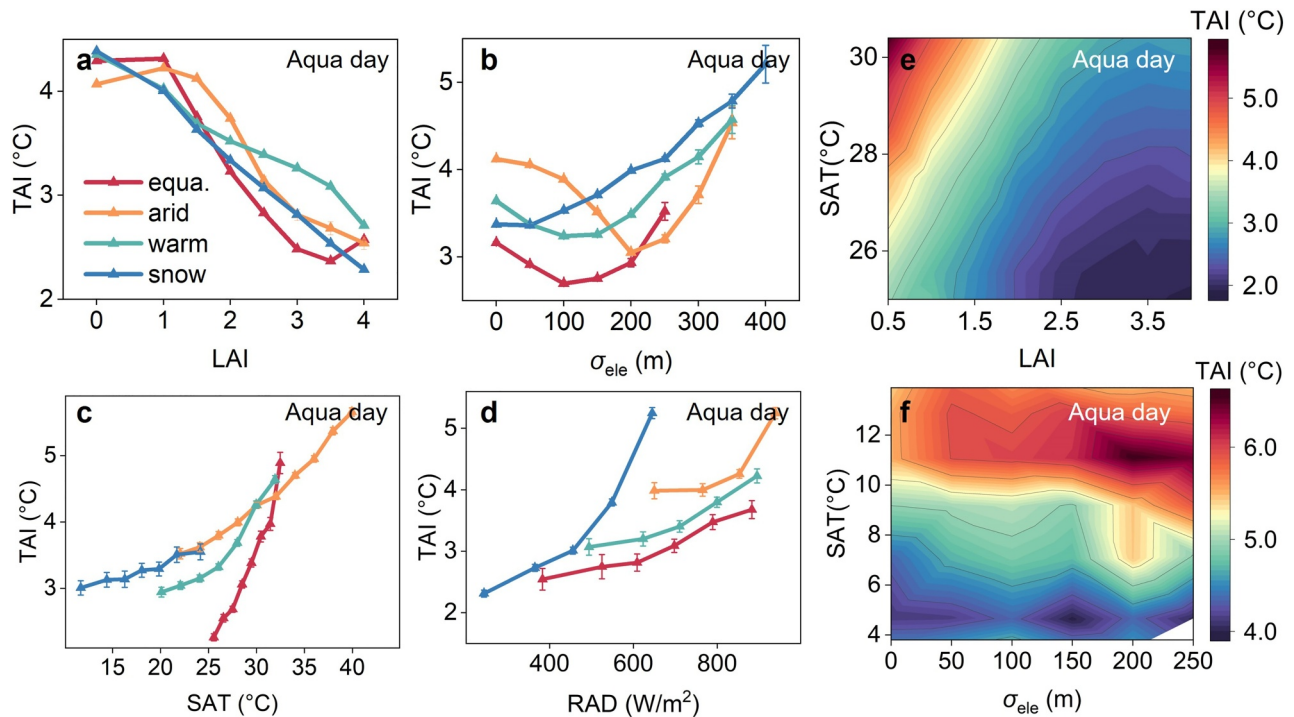


**Figure 3.** Variations in global land surface TAI depending on typical surface and atmospheric parameters during summer afternoon. Variations in TAI with leaf area index (LAI) across different climatic zones (a); variations in TAI with elevation standard deviation ( $\sigma_{ele}$ ) over mountainous surfaces (b); variations in TAI with surface air temperature (SAT; c) and downward shortwave radiation (RAD; d); variations in TAI with interactive effects of LAI and SAT in tropical climate zone (e); variations in TAI with interactive effects of  $\sigma_{ele}$  and SAT over the Tibetan Plateau (f). This figure shows the results for summer afternoon, and additional results for summer morning are presented in Figures S13–S18 in Supporting Information S1. Reasons for the relatively low RAD values in panel (d) are provided in Text S7 in Supporting Information S1.

instance, variations in TAI exhibit a strong correlation with both LAI and SAT in tropical regions (Figure 3e; Figure S18 in Supporting Information S1). Specifically, TAI increases from 2.0°C under conditions of lower SAT and larger LAI to 6.4°C under higher SAT and lower LAI (Figure 3e). Similarly, a strong correlation exists between variations in TAI,  $\sigma_{ele}$ , and SAT over the Tibetan Plateau, with TAI ranging from 3.7°C to 6.1°C from lower to higher SAT and  $\sigma_{ele}$  values (Figure 3f; Figure S18 in Supporting Information S1). These correlations provide valuable insights for performing practical angular normalization of thermal anisotropy across global lands (see Discussion and concluding remarks).

#### 4. Discussion and Concluding Remarks

For over half a century, physical and semi-physical models, alongside recently formulated multi-source data-driven approaches, have been effectively used to map surface thermal anisotropy for specific land cover types and time periods. However, these previous methods typically necessitate either restrictive assumptions on surface temperature dynamics or additional ground-based observations, significantly constraining their widespread spatiotemporal applicability (Text S1 in Supporting Information S1). Our single-source data-driven approach overcomes these limitations by harnessing only an historical archive of satellite thermal observations (see Materials and methods), enabling the first comprehensive global mapping of thermal anisotropy. The core of our approach lies in the extensive spatiotemporal averaging of these vast satellite observation archives, which well suppresses the impact of rapid atmospheric fluctuations, as specified by the Bessel formula in classical error theory (Pugachev, 2014).

Compared to previous physical and semi-physical models, our single-source data-driven approach presents the following advantages. (a) Independence from elaborate surface information: Differing from physical models, our approach only requires time series LST data observations from polar orbiters for mapping, during which elaborate surface structure and property information is unnecessary as model input. (b) Independence from restrictive

assumptions on diurnal LST cycle patterns: Differing from semi-physical models, our mapping processes each satellite overpass individually, avoiding the reliance on diurnal LST cycle models or geostationary satellite data. Compared to previous multi-source data-driven approaches, our approach offers several key advancements. (a) Independence from water bodies: Unlike prior studies that relied on adjacent water bodies as a reference to mitigate the impact of varying atmospheric conditions, our method bypasses the need for such references and directly maps directional thermal radiation through comprehensive spatial and temporal averaging of LST within each zenith angle interval. (b) Ground-based data independence: Our approach relies solely on satellite data and eliminates the need for ground-based LST observations, overcoming limitations associated with uneven distribution of ground-based LST observation sites. By overcoming these above-mentioned limitations, our approach achieved genuine global thermal anisotropy mapping. While a previous version of the single-source data-driven approach was successfully applied to urban areas characterized by high TAI (Du et al., 2023), this current study formulated a more advanced and holistic framework for global-scale analysis (Figure S1 in Supporting Information S1). This advancement enables the production of global TAI maps and direct angular correction of MODIS LSTs using the established relationships (Figure 3).

By generating the first global land surface map of TAI, we reveal pronounced seasonal and diurnal variations in TAI across global lands, with a global mean TAI of 2.8°C during summer days (Figures 1a and 1b). This value is approximately half the 5.1 K observed in highly heterogeneous urban environments worldwide during the same period (Du et al., 2023). Moreover, we identify exceptionally high TAI values exceeding 7.0°C in arid zone deserts (Figure 2). Such significant anisotropy could translate significant errors into calculations of surface longwave radiation (~10%) and latent heat flux (~32%) when thermal observations are not corrected for anisotropy (Hu et al., 2023; Jiang et al., 2022). These findings fill an essential knowledge gap regarding the complex spatiotemporal dynamics of TAI. Our results also confirm the established relationships between LAI and TAI as observed over small-scale vegetated surfaces in previous studies also hold true across all climate zones globally (Figure 3). Despite previous expectation of topography's impacts, we further find a strong correlation between TAI and elevation variability in global mountainous regions. Furthermore, we identify interactive effects between surface and atmospheric variables on TAI (Figure 3). These findings pave the foundation for developing correction models to address the directional bias inherent in satellite-derived LSTs. By considering the interplay of satellite-derived LST variations at differing viewing angles and these associated parameters, we can construct correction models applicable to all terrestrial landscapes (vegetated, urban, snow-covered, and barren). Importantly, the establishment requires neither complex physical modeling nor additional data beyond the readily available archives of MODIS and reanalysis products.

Using MODIS products, we have demonstrated the effectiveness of a purely data-driven approach to global thermal anisotropy mapping. Our methodology can be adapted to other multi-angle thermal instruments onboard polar-orbiters with enough daily coverage (e.g., Suomi-NPP VIIRS, Sentinel-3 SLSTR). However, we acknowledge that the limited azimuthal view of MODIS precludes comprehensive mapping within the entire upper hemisphere (Hu et al., 2016). Furthermore, while our endeavor is rooted in a single-source data-driven paradigm, we recognize the complementary values of physical modeling and multi-source data integration for a more thorough comprehension of hemispheric thermal anisotropy. In summary, our findings advocate for a new era of data-centric exploration to advance thermal anisotropy studies, aligning with the broader paradigm shift toward data-intensive research in Earth sciences (Reichstein et al., 2019).

### Conflict of Interest

The authors declare no conflicts of interest relevant to this study.

### Data Availability Statement

The multi-angle land surface temperature (LST) data from the MOD11A1 and MYD11A1 products are publicly available at [https://developers.google.com/earth-engine/datasets/catalog/MODIS\\_061\\_MOD11A1](https://developers.google.com/earth-engine/datasets/catalog/MODIS_061_MOD11A1) (Wan et al., 2021a) and [https://developers.google.com/earth-engine/datasets/catalog/MODIS\\_061\\_MYD11A1](https://developers.google.com/earth-engine/datasets/catalog/MODIS_061_MYD11A1) (Wan et al., 2021b), respectively. The leaf area index (LAI) data from the MCD15A3H product are publicly obtainable at [https://developers.google.com/earth-engine/datasets/catalog/MODIS\\_061\\_MCD15A3H](https://developers.google.com/earth-engine/datasets/catalog/MODIS_061_MCD15A3H) (Myneni et al., 2021). The enhanced vegetation index (EVI) data from the MOD13A2 product are publicly obtainable at <https://>

developers.google.com/earth-engine/datasets/catalog/MODIS\_061\_MOD13A2 (Didan, 2021). The tree cover percentage (TCP) data from the MOD44B product are publicly obtainable at [https://developers.google.com/earth-engine/datasets/catalog/MODIS\\_006\\_MOD44B](https://developers.google.com/earth-engine/datasets/catalog/MODIS_006_MOD44B) (DiMiceli et al., 2015). The elevation data from the SRTMGL1\_003 product are publicly obtainable at [https://developers.google.com/earth-engine/datasets/catalog/USGS\\_SRTMGL1\\_003](https://developers.google.com/earth-engine/datasets/catalog/USGS_SRTMGL1_003) (NASA JPL, 2013). The hourly downward shortwave radiation (RAD) and surface air temperature (SAT) data provided by the reanalysis ERA5-land product are publicly obtainable at [https://developers.google.com/earth-engine/datasets/catalog/ECMWF\\_ERA5\\_LAND\\_HOURLY?hl=en](https://developers.google.com/earth-engine/datasets/catalog/ECMWF_ERA5_LAND_HOURLY?hl=en) (Muñoz Sabater, 2019).

### Acknowledgments

We gratefully acknowledge the National Natural Science Foundation of China (42171306), the Fundamental Research Funds for the Central Universities (2024300388), and the National Natural Science Foundation of China (423B2105 and 42201337) for supporting this current study. We also thank the support from the National Youth Talent Support Program of China, and Ms. Shasha Wang for her valuable comments in the process of addressing the reviewers' comments.

### References

- Alexandridis, T. K., Ovakoglou, G., & Clevers, J. G. (2020). Relationship between MODIS EVI and LAI across time and space. *Geocarto International*, 35, 1385–1399.
- Bian, Z. J., Zhong, S. Y., Roujean, J.-L., Liu, X. Y., Duan, S. B., Li, H., et al. (2024). An integrated method for angular and temporal reconstruction of land surface temperatures. *Remote Sensing of Environment*, 313, 114357. <https://doi.org/10.1016/j.rse.2024.114357>
- Cao, B., Liu, Q. H., Du, Y. M., Roujean, J.-L., Gastellu-Etchegorry, J.-P., Trigo, I. F., et al. (2019). A review of earth surface thermal radiation directionality observing and modeling: Historical development, current status and perspectives. *Remote Sensing of Environment*, 232, 111304. <https://doi.org/10.1016/j.rse.2019.111304>
- Cao, B., Roujean, J.-L., Gastellu-Etchegorry, J.-P., Liu, Q. H., Du, Y. M., Lagouarde, J.-P., et al. (2021). A general framework of kernel-driven modeling in the thermal infrared domain. *Remote Sensing of Environment*, 252, 112157. <https://doi.org/10.1016/j.rse.2020.112157>
- Chakraborty, T., & Qian, Y. (2024). Urbanization exacerbates continental-to regional-scale warming. *One Earth*, 7(8), 1387–1401. <https://doi.org/10.1016/j.oneear.2024.05.005>
- Didan, K. (2021). MODIS/Terra vegetation indices 16-day L3 global 1km SIN Grid V061 [Dataset]. *NASA EOSDIS Land Processes Distributed Active Archive Center*. <https://doi.org/10.5067/MODIS/MOD13A2.061>
- DiMiceli, C., Carroll, M., Sohlberg, R., Kim, D., Kelly, M., & Townshend, J. (2015). MOD44B MODIS/Terra vegetation continuous fields yearly L3 Global 250m SIN grid V006 [Dataset]. *NASA EOSDIS Land Processes Distributed Active Archive Center*. <https://doi.org/10.5067/MODIS/MOD44B.006>
- Du, H. L., Zhan, W. F., Liu, Z. H., Krayenhoff, E. S., Chakraborty, T. C., Zhao, L., et al. (2023). Global mapping of urban thermal anisotropy reveals substantial potential biases for remotely sensed urban climates. *Science Bulletin*, 68(16), 1809–1818. <https://doi.org/10.1016/j.scib.2023.06.032>
- Duffour, C., Lagouarde, J. P., & Roujean, J. L. (2016). A two parameter model to simulate thermal infrared directional effects for remote sensing applications. *Remote Sensing of Environment*, 186, 250–261. <https://doi.org/10.1016/j.rse.2016.08.012>
- Ermida, S. L., DaCamara, C. C., Trigo, I. F., Pires, A. C., Ghent, D., & Remedios, J. (2017). Modelling directional effects on remotely sensed land surface temperature. *Remote Sensing of Environment*, 190, 56–69. <https://doi.org/10.1016/j.rse.2016.12.008>
- Ermida, S. L., Hulley, G., & Trigo, I. F. (2024). Introducing emissivity directionality to the temperature-emissivity separation algorithm. *Remote Sensing of Environment*, 311, 114280. <https://doi.org/10.1016/j.rse.2024.114280>
- Ermida, S. L., Trigo, I. F., DaCamara, C. C., & Roujean, J.-L. (2018). Assessing the potential of parametric models to correct directional effects on local to global remotely sensed LST. *Remote Sensing of Environment*, 209, 410–422. <https://doi.org/10.1016/j.rse.2018.02.066>
- Hu, L. Q., Monaghan, A., Voogt, J. A., & Barlage, M. (2016). A first satellite-based observational assessment of urban thermal anisotropy. *Remote Sensing of Environment*, 181, 111–121. <https://doi.org/10.1016/j.rse.2016.03.043>
- Hu, T., Roujean, J.-L., Cao, B., Mallick, K., Boulet, G., Li, H., et al. (2023). Correction for LST directionality impact on the estimation of surface upwelling longwave radiation over vegetated surfaces at the satellite scale. *Remote Sensing of Environment*, 295, 113649. <https://doi.org/10.1016/j.rse.2023.113649>
- Jiang, L., Zhan, W. F., Voogt, J. A., Zhao, L. M., Gao, L., Huang, F., et al. (2018). Remote estimation of complete urban surface temperature using only directional radiometric temperatures. *Building and Environment*, 135, 224–236. <https://doi.org/10.1016/j.buildenv.2018.03.005>
- Jiang, Y. Z., Tang, R. L., & Li, Z. L. (2022). A framework of correcting the angular effect of land surface temperature on evapotranspiration estimation in single-source energy balance models. *Remote Sensing of Environment*, 283, 113306. <https://doi.org/10.1016/j.rse.2022.113306>
- Jiao, Z. H., Yan, G. J., Wang, T. X., Mu, X. H., & Zhao, J. (2019). Modeling of land surface thermal anisotropy based on directional and equivalent brightness temperatures over complex terrain. *Ieee Journal of Selected Topics in Applied Earth Observations and Remote Sensing*, 12(2), 410–423. <https://doi.org/10.1109/jstars.2018.2855192>
- Li, Z. L., Wu, H., Duan, S. B., Zhao, W., Ren, H. Z., Liu, X. Y., et al. (2023). Satellite remote sensing of global land surface temperature: Definition, methods, products, and applications. *Reviews of Geophysics*, 61(1), e2022RG000777. <https://doi.org/10.1029/2022rg000777>
- Michel, J., Hagolle, O., Hook, S. J., Roujean, J.-L., & Gamet, P. (2023). Quantifying Thermal Infra-Red directional anisotropy using Master and Landsat-8 simultaneous acquisitions. *Remote Sensing of Environment*, 297, 113765. <https://doi.org/10.1016/j.rse.2023.113765>
- Mildrexler, D. J., Zhao, M. S., & Running, S. W. (2011). Satellite finds highest land skin temperatures on Earth. *Bulletin of the American Meteorological Society*, 92(7), 855–860. <https://doi.org/10.1175/2011bams3067.1>
- Monteith, J. L., & Szeicz, G. (1962). Radiative temperature in the heat balance of natural surfaces. *Quarterly Journal of the Royal Meteorological Society*, 88(378), 496–507. <https://doi.org/10.1002/qj.49708837811>
- Muñoz Sabater, J. (2019). ERA5-Land monthly averaged data from 1950 to present [Dataset]. *Copernicus Climate Change Service (C3S) Climate Data Store (CDS)*. <https://doi.org/10.24381/cds.68d2bb30>
- Myneni, R., Knyazikhin, Y., & Park, T. (2021). MODIS/Terra+Aqua leaf area index/FPAR 4-day L4 global 500m SIN grid V061 [Dataset]. *NASA EOSDIS Land Processes Distributed Active Archive Center*. <https://doi.org/10.5067/MODIS/MCD15A3H.061>
- NASA JPL. (2013). NASA shuttle radar topography mission global 1 arc second [Dataset]. *NASA EOSDIS Land Processes Distributed Active Archive Center*. <https://doi.org/10.5067/MEASUREs/SRTM/SRTMGL1.003>
- Pugachev, V. S. (2014). *Probability theory and mathematical statistics for engineers*. Elsevier.
- Qin, B. X., Chen, S. S., Cao, B., Yu, Y. Y., Yu, P., Na, Q., et al. (2025). Angular normalization of GOES-16 and GOES-17 land surface temperature over overlapping region using an extended time-evolving kernel-driven model. *Remote Sensing of Environment*, 318, 114532. <https://doi.org/10.1016/j.rse.2024.114532>

- Rasmussen, M. O., Pinheiro, A. C., Proud, S. R., & Sandholt, I. (2010). Modeling angular dependences in land surface temperatures from the SEVIRI instrument onboard the geostationary Meteosat Second Generation satellites. *IEEE Transactions on Geoscience and Remote Sensing*, 48(8), 3123–3133. <https://doi.org/10.1109/tgrs.2010.2044509>
- Reichstein, M., Camps-Valls, G., Stevens, B., Jung, M., Denzler, J., Carvalhais, N., & Prabhat (2019). Deep learning and process understanding for data-driven Earth system science. *Nature*, 566(7743), 195–204. <https://doi.org/10.1038/s41586-019-0912-1>
- Schaaf, C. B., Gao, F., Strahler, A. H., Lucht, W., Li, X. W., Tsang, T., et al. (2002). First operational BRDF, albedo nadir reflectance products from MODIS. *Remote Sensing of Environment*, 83(1–2), 135–148. [https://doi.org/10.1016/s0034-4257\(02\)00091-3](https://doi.org/10.1016/s0034-4257(02)00091-3)
- Schwaab, J., Meier, R., Mussetti, G., Seneviratne, S., Bürgi, C., & Davin, E. L. (2021). The role of urban trees in reducing land surface temperatures in European cities. *Nature Communications*, 12(1), 6763. <https://doi.org/10.1038/s41467-021-26768-w>
- Stewart, I. D., & Oke, T. R. (2012). Local climate zones for urban temperature studies. *Bulletin of the American Meteorological Society*, 93(12), 1879–1900. <https://doi.org/10.1175/bams-d-11-00019.1>
- Teng, Y. J., Ren, H. Z., Zhu, J. S., Jiang, C. C., Ye, X., & Zeng, H. (2023). A practical method for angular normalization on land surface temperature using space between thermal radiance and fraction of vegetation cover. *Remote Sensing of Environment*, 291, 113558. <https://doi.org/10.1016/j.rse.2023.113558>
- Trigo, I. F., Monteiro, I. T., Olesen, F., & Kabsch, E. (2008). An assessment of remotely sensed land surface temperature. *Journal of Geophysical Research*, 113(D17), D17108. <https://doi.org/10.1029/2008jd010035>
- Wan, Z. M., Hook, S., & Hulley, G. (2021a). MODIS/Terra land surface temperature/emissivity daily L3 global 1km SIN grid V061 [Dataset]. NASA EOSDIS Land Processes Distributed Active Archive Center. <https://doi.org/10.5067/MODIS/MOD11A1.061>
- Wan, Z. M., Hook, S., & Hulley, G. (2021b). MODIS/Aqua land surface temperature/emissivity daily L3 global 1km SIN grid V061 [Dataset]. NASA EOSDIS Land Processes Distributed Active Archive Center. <https://doi.org/10.5067/MODIS/MYD11A1.061>
- Wang, D. D., Chen, Y. H., Hu, L. Q., Voogt, J. A., & He, X. Y. (2022). Satellite-based daytime urban thermal anisotropy: A comparison of 25 global cities. *Remote Sensing of Environment*, 283, 113312. <https://doi.org/10.1016/j.rse.2022.113312>
- Wang, J. R., Tang, R. L., Jiang, Y. Z., Liu, M., & Li, Z. L. (2023). A practical method for angular normalization of global MODIS land surface temperature over vegetated surfaces. *ISPRS Journal of Photogrammetry and Remote Sensing*, 199, 289–304. <https://doi.org/10.1016/j.isprsjrs.2023.04.015>
- Yan, G. J., Wang, T. X., Jiao, Z. H., Mu, X. H., Zhao, J., & Chen, L. (2016). Topographic radiation modeling and spatial scaling of clear-sky land surface longwave radiation over rugged terrain. *Remote Sensing of Environment*, 172, 15–27. <https://doi.org/10.1016/j.rse.2015.10.026>

## References From the Supporting Information

- Bian, Z. J., Cao, B., Li, H., Du, Y. M., Fan, W. J., Xiao, Q., & Liu, Q. (2020). The effects of tree trunks on the directional emissivity and brightness temperatures of a leaf-off forest using a geometric optical model. *IEEE Transactions on Geoscience and Remote Sensing*, 59(6), 5370–5386. <https://doi.org/10.1109/tgrs.2020.3011157>
- Bian, Z. J., Cao, B., Li, H., Du, Y. M., Lagouarde, J.-P., Xiao, Q., & Liu, Q. (2018). An analytical four-component directional brightness temperature model for crop and forest canopies. *Remote Sensing of Environment*, 209, 731–746. <https://doi.org/10.1016/j.rse.2018.03.010>
- Bian, Z. J., Roujean, J.-L., Cao, B., Du, Y. M., Li, H., Gamet, P., et al. (2021). Modeling the directional anisotropy of fine-scale TIR emissions over tree and crop canopies based on UAV measurements. *Remote Sensing of Environment*, 252, 112150. <https://doi.org/10.1016/j.rse.2020.112150>
- Bonamente, M. (2017). *Statistics and analysis of scientific data*. Springer.
- Chen, C., Park, T., Wang, X. H., Piao, S. L., Xu, B. D., Chaturvedi, R. K., et al. (2019). China and India lead in greening of the world through land-use management. *Nature Sustainability*, 2, 122–129. <https://doi.org/10.1038/s41893-019-0220-7>
- Coll, C., Galve, J. M., Niclòs, R., Valor, E., & Barberà, M. J. (2019). Angular variations of brightness surface temperatures derived from dual-view measurements of the Advanced Along-Track Scanning Radiometer using a new single band atmospheric correction method. *Remote Sensing of Environment*, 223, 274–290. <https://doi.org/10.1016/j.rse.2019.01.021>
- Crosson, W. L., Al-Hamdan, M. Z., Hemmings, S. N., & Wade, G. M. (2012). A daily merged MODIS Aqua–Terra land surface temperature data set for the conterminous United States. *Remote Sensing of Environment*, 119, 315–324. <https://doi.org/10.1016/j.rse.2011.12.019>
- Diego Delso. (2018). CC BY-SA 4.0 Retrieved from <https://creativecommons.org/licenses/by-sa/4.0/viaWikimediaCommons>. [https://commons.wikimedia.org/wiki/File:Duna\\_en\\_Sossusvlei\\_Namibia\\_2018-08-06\\_DD\\_002.jpg](https://commons.wikimedia.org/wiki/File:Duna_en_Sossusvlei_Namibia_2018-08-06_DD_002.jpg)
- Du, Y. M., Liu, Q. H., Chen, L. F., Liu, Q., & Yu, T. (2007). Modeling directional brightness temperature of the winter wheat canopy at the ear stage. *IEEE Transactions on Geoscience and Remote Sensing*, 45(11), 3721–3739. <https://doi.org/10.1109/tgrs.2007.903401>
- Duffour, C., Lagouarde, J.-P., Olioso, A., Demarty, J., & Roujean, J.-L. (2016b). Driving factors of the directional variability of thermal infrared signal in temperate regions. *Remote Sensing of Environment*, 177, 248–264. <https://doi.org/10.1016/j.rse.2016.02.024>
- Dyce, D. R., & Voogt, J. A. (2018). The influence of tree crowns on urban thermal effective anisotropy. *Urban Climate*, 23, 91–113. <https://doi.org/10.1016/j.uclim.2017.02.006>
- Gong, P., Li, X. C., Wang, J., Bai, Y. Q., Chen, B., Hu, T. Y., et al. (2020). Annual maps of global artificial impervious area (GAIA) between 1985 and 2018. *Remote Sensing of Environment*, 236, 111510. <https://doi.org/10.1016/j.rse.2019.111510>
- García-Santos, V., Coll, C., Valor, E., Niclòs, R., & Caselles, V. (2015). Analyzing the anisotropy of thermal infrared emissivity over arid regions using a new MODIS land surface temperature and emissivity product (MOD21). *Remote Sensing of Environment*, 169, 212–221. <https://doi.org/10.1016/j.rse.2015.07.031>
- Hu, T., Renzullo, L. J., Cao, B., van Dijk, A. I., Du, Y. M., Li, H., et al. (2019). Directional variation in surface emissivity inferred from the MYD21 product and its influence on estimated surface upwelling longwave radiation. *Remote Sensing of Environment*, 228, 45–60. <https://doi.org/10.1016/j.rse.2019.04.012>
- Huang, H. G., Liu, Q. H., Qin, W. H., Du, Y. M., & Li, X. W. (2011). Temporal patterns of thermal emission directionality of crop canopies. *Journal of Geophysical Research*, 116(D6), D06114. <https://doi.org/10.1029/2010jd014613>
- Jacob, F., Schmugge, T., Olioso, A., French, A., Courault, D., Ogawa, K., et al. (2008). Modeling and inversion in thermal infrared remote sensing over vegetated land surfaces. *Advances in land remote sensing: System, modeling, inversion and application*, 245–291. [https://doi.org/10.1007/978-1-4020-6450-0\\_10](https://doi.org/10.1007/978-1-4020-6450-0_10)
- Jiang, L., Zhan, W. F., Hu, L. Q., Huang, F., Hong, F. L., Liu, Z. H., et al. (2021). Assessment of different kernel-driven models for daytime urban thermal radiation directionality simulation. *Remote Sensing of Environment*, 263, 112562. <https://doi.org/10.1016/j.rse.2021.112562>
- Kimes, D. S., Idso, S., Pinter Jr, P., Reginato, R., & Jackson, R. (1980). View angle effects in the radiometric measurement of plant canopy temperatures. *Remote Sensing of Environment*, 10(4), 273–284. [https://doi.org/10.1016/0034-4257\(80\)90087-5](https://doi.org/10.1016/0034-4257(80)90087-5)

- Kimes, D. S., & Kirchner, J. A. (1983). Directional radiometric measurements of row-crop temperatures. *International Journal of Remote Sensing*, 4(2), 299–311. <https://doi.org/10.1080/01431168308948548>
- Krayenhoff, E. S., & Voogt, J. A. (2016). Daytime thermal anisotropy of urban neighbourhoods: Morphological causation. *Remote Sensing*, 8(2), 108. <https://doi.org/10.3390/rs8020108>
- Lagouarde, J. P., Hénon, A., Irvine, M., Voogt, J. A., Pigeon, G., Moreau, P., et al. (2012). Experimental characterization and modelling of the nighttime directional anisotropy of thermal infrared measurements over an urban area: Case study of Toulouse (France). *Remote Sensing of Environment*, 117, 19–33. <https://doi.org/10.1016/j.rse.2011.06.022>
- Lagouarde, J. P., Hénon, A., Kurz, B., Moreau, P., Irvine, M., Voogt, J. A., & Mestayer, P. (2010). Modelling daytime thermal infrared directional anisotropy over Toulouse city centre. *Remote Sensing of Environment*, 114(1), 87–105. <https://doi.org/10.1016/j.rse.2009.08.012>
- Lipton, A. E., & Ward, J. M. (1997). Satellite-view biases in retrieved surface temperatures in mountain areas. *Remote Sensing of Environment*, 60(1), 92–100. [https://doi.org/10.1016/s0034-4257\(96\)00165-4](https://doi.org/10.1016/s0034-4257(96)00165-4)
- Liu, X. Y., Tang, B. H., & Li, Z. L. (2018). Evaluation of three parametric models for estimating directional thermal radiation from simulation, airborne, and satellite data. *Remote Sensing*, 10(3), 420. <https://doi.org/10.3390/rs10030420>
- Morrison, W., Grimmond, S., & Kotthaus, S. (2023). Simulating satellite urban land surface temperatures: Sensitivity to sensor view angle and assumed landscape complexity. *Remote Sensing of Environment*, 293, 113579. <https://doi.org/10.1016/j.rse.2023.113579>
- Na, Q., Cao, B., Qin, B. X., Mo, F., Zheng, L. M., Du, Y. M., et al. (2024). Correcting an off-nadir to a nadir land surface temperature using a multitemporal thermal infrared kernel-driven model during daytime. *Remote Sensing*, 16(10), 1790. <https://doi.org/10.3390/rs16101790>
- Na, Q., Li, H., Cao, B., Qin, B. X., Zheng, L. M., Bian, Z. J., et al. (2024). Comprehensive analysis of current 1-km land surface temperature products in sparsely vegetated area: T-Based evaluation, thermal anisotropy and joint application. *IEEE Transactions on Geoscience and Remote Sensing*, 62, 1–14. <https://doi.org/10.1109/tgrs.2024.3418964>
- Paw U, K. T. (1992). Development of models for thermal infrared radiation above and within plant canopies. *ISPRS Journal of Photogrammetry and Remote Sensing*, 47(2–3), 189–203. [https://doi.org/10.1016/0924-2716\(92\)90032-5](https://doi.org/10.1016/0924-2716(92)90032-5)
- Pinheiro, A. C., Privette, J. L., & Guillevic, P. (2006). Modeling the observed angular anisotropy of land surface temperature in a savanna. *IEEE Transactions on Geoscience and Remote Sensing*, 44(4), 1036–1047. <https://doi.org/10.1109/tgrs.2005.863827>
- Pinheiro, A. C., Privette, J. L., Mahoney, R., & Tucker, C. J. (2004). Directional effects in a daily AVHRR land surface temperature dataset over Africa. *IEEE Transactions on Geoscience and Remote Sensing*, 42(9), 1941–1954. <https://doi.org/10.1109/tgrs.2004.831886>
- Qin, B. X., Cao, B., Roujean, J.-L., Gastellu-Etchegorry, J.-P., Ermida, S. L., Bian, Z. J., et al. (2023). A thermal radiation directionality correction method for the surface upward longwave radiation of geostationary satellite based on a time-evolving kernel-driven model. *Remote Sensing of Environment*, 294, 113599. <https://doi.org/10.1016/j.rse.2023.113599>
- Ragnhild & Neil. (2015). CC BY-SA 2.0 Retrieved from <https://creativecommons.org/licenses/by-sa/2.0/viaWikimediaCommons>. [https://commons.wikimedia.org/wiki/File:Sossusvlei-3728\\_-\\_Flickr\\_-\\_Ragnhild\\_%26\\_Neil\\_Crawford.jpg](https://commons.wikimedia.org/wiki/File:Sossusvlei-3728_-_Flickr_-_Ragnhild_%26_Neil_Crawford.jpg)
- Rasmussen, M. O., Göttsche, F.-M., Olesen, F.-S., & Sandholt, I. (2011). Directional effects on land surface temperature estimation from Meteosat Second Generation for savanna landscapes. *IEEE Transactions on Geoscience and Remote Sensing*, 49(11), 4458–4468. <https://doi.org/10.1109/tgrs.2011.2144604>
- Sneathlge, M. A., Geschke, J., Ranipeta, A., Jetz, W., Yoccoz, N. G., Körner, C., et al. (2022). A hierarchical inventory of the world's mountains for global comparative mountain science. *Scientific Data*, 9(1), 149. <https://doi.org/10.1038/s41597-022-01256-y>
- Vinnikov, K. Y., Yu, Y. Y., Goldberg, M. D., Tarpley, D., Romanov, P., Laszlo, I., & Chen, M. (2012). Angular anisotropy of satellite observations of land surface temperature. *Geophysical Research Letters*, 39(23), L23802. <https://doi.org/10.1029/2012gl054059>
- Wan, Z. M. (2014). New refinements and validation of the collection-6 MODIS land-surface temperature/emissivity product. *Remote Sensing of Environment*, 140, 36–45. <https://doi.org/10.1016/j.rse.2013.08.027>
- Wang, D. D., Chen, Y. H., Voogt, J. A., Krayenhoff, E. S., Wang, J. F., & Wang, L. B. (2020). An advanced geometric model to simulate thermal anisotropy time-series for simplified urban neighborhoods (GUTA-T). *Remote Sensing of Environment*, 237, 111547. <https://doi.org/10.1016/j.rse.2019.111547>
- Wang, D. D., Chen, Y. H., & Zhan, W. F. (2018). A geometric model to simulate thermal anisotropy over a sparse urban surface (GUTA-sparse). *Remote Sensing of Environment*, 209, 263–274. <https://doi.org/10.1016/j.rse.2018.02.051>
- Wang, X. H., Luo, S. W., Liu, X. N., Ren, Z. H., & Sun, H. N. (2006). Quality control and software development about A-format data of national basic automatic weather station. *Meteorological Monthly*, 32, 107–112.
- Xiao, Y., Yuan, Q. Q., Jiang, K., Chen, Y. Z., Zhang, Q., & Lin, C. W. (2024). Frequency-assisted mamba for remote sensing image super-resolution. *IEEE Transactions on Multimedia*, 27, 1783–1796. <https://doi.org/10.1109/TMM.2024.3521798>